

<https://doi.org/10.1038/s42004-025-01537-8>

Structural convergence and membrane interactions of A β ₁₋₄₂ along the primary nucleation process studied by solid state NMR



Maurine K. Kengwerere¹, June M. Kenyaga¹, Peng Xiao², Shubha S. Gunaga³, Faith J. Scott³, Xyomara Wutoh-Hughes¹, James Wang¹, Brian Lum¹, Yan Sun⁴, Frederic Mentink-Vigier^{3,5}, Tuo Wang² & Wei Qiang¹ ✉

Non-specific disruption of cellular membranes induced by amyloidogenic aggregation of β -amyloid (A β) peptides remains a viable cytotoxicity mechanism in Alzheimer's disease (AD). Obtaining structural information about the intermediate states of A β -membrane systems and their molecular interactions is challenging due to their heterogeneity and low abundance. Here, we systematically study the molecular interactions of membrane-associated A β ₁₋₄₂ peptides using solid-state nuclear magnetic resonance (ssNMR) spectroscopy, focusing on the primary nucleation phase of the fibrillation process. Compared to the less pathogenic A β ₁₋₄₀ peptide, A β ₁₋₄₂ forms smaller oligomers prior to fibrillation, as evidenced by a higher overall population of lipid-proximity peptides. A β ₁₋₄₂ also exhibits more pronounced residue-specific contacts with phospholipid headgroups compared to A β ₁₋₄₀, with multiple lipid-proximity segments throughout the entire primary sequence. The segments involved in initial inter-strand assembly overlap with those located near the lipid headgroups in A β ₁₋₄₂, whereas these two segments are distinct in A β ₁₋₄₀. ssNMR spectroscopy with sensitivity enhanced by Dynamic nuclear polarization (DNP) confirmed local secondary structural convergence during the nucleation process of A β ₁₋₄₂ and the presence of long-range tertiary contacts at early stages of nucleation. Overall, our results provide a molecular-level understanding of the A β ₁₋₄₂ nucleation process in a membrane-like environment and its membrane-disrupting intermediates. The comparison between A β ₁₋₄₂ and A β ₁₋₄₀ explains its higher cytotoxicity from the perspective of membrane disruption.

Non-specific membrane disruption induced by extracellular β -amyloid (A β) aggregates is considered a tenable mechanism of A β cytotoxicity and pathology in Alzheimer's disease (AD)¹⁻³. Upon enzymatic cleavage of the amyloid precursor protein, the released A β is likely to initiate aggregation at the membrane surface and within the extracellular matrix. Pathological amyloid plaques are commonly associated with lipids, sterols, and extracellular proteins⁴⁻⁶. Recent updates to the amyloid cascade hypothesis (ACH) highlight cellular plasma membranes as a platform for the co-

aggregation of multiple amyloidogenic proteins, such as the coaggregation between A β and tau, which may be more directly relevant to AD pathology^{4,7-9}. Despite its biological importance, understanding the molecular structural features and membrane interactions of A β intermediate states during the primary nucleation stage remains a major challenge¹⁰⁻¹³.

Current experimental studies on the nucleation intermediate states of A β fibrillation primarily use kinetic assays and microscopic techniques. The kinetic assays provide insights into the molecular mechanisms of nucleation,

¹Department of Chemistry, Binghamton University, State University of New York, Binghamton, NY, USA. ²Department of Chemistry, Michigan State University, East Lansing, MI, USA. ³National High Magnetic Field Laboratory, Florida State University, Tallahassee, FL, USA. ⁴Small Scale System Integration and Packaging (S3IP), Binghamton University, Binghamton, NY, USA. ⁵Department of Chemistry and Biochemistry, Florida State University, Tallahassee, FL, USA.

✉ e-mail: wqiang@binghamton.edu

including the involvement of multistep nucleation processes, the rates of individual steps, and potential critical oligomer sizes. For instance, a recent kinetic study suggested that $A\beta_{1-42}$ may adopt two distinct nucleation mechanisms at varying initial monomeric concentration, with a predicted critical nucleus size of seven to eight monomers¹⁴. Kinetic studies have also revealed distinct nucleation mechanisms in $A\beta_{1-40}$ and $A\beta_{1-42}$, particularly regarding the dominance of secondary nucleation¹⁵. Microscopic studies enable direct observation of the presence, morphology, and interactions of $A\beta$ intermediates during nucleation processes. For instance, a previous atomic force microscopy (AFM) study showed that the N-terminal segments of $A\beta$ preferentially bind to ganglioside-enriched membrane domains, while the C-terminal segments serve as anchors to the bilayer interior through hydrophobic interactions¹⁶. Single-molecule microscopy also directly observes the attachment of $A\beta$ monomers and low-order oligomers to fibrillar surfaces through the secondary nucleation process¹⁷. Complementary to the experimental findings, computational simulations provide insights into residue-specific interactions between $A\beta$ and membrane compositions during nucleation. A recent all-atom molecular dynamics (MD) simulation highlighted the presence and membrane interactions of an $A\beta_{1-42}$ dimer during the nucleation phase in phosphatidylcholine bilayers and proposed the formation of an F19-F20 π - π ring stacking and a D23-K28 salt bridge in this early-stage dimeric intermediate¹⁸. Currently, there is limited residue-specific experimental information available regarding the membrane-associated $A\beta_{1-42}$ nucleation intermediate states.

Solid-state nuclear magnetic resonance (ssNMR) spectroscopy has been widely used to characterize the molecular structure and dynamics of $A\beta$ fibrils and stable oligomers, providing a highly effective approach for exploring the residue-specific features of $A\beta$ -membrane nucleation intermediates. The current study examined site-specific interstrand distances in membrane-associated $A\beta_{1-42}$ intermediate states and their proximities to lipid phosphate groups, using ^{13}C -PITHIRDS-CT¹⁹ and ^{13}C - ^{31}P REDOR²⁰ ssNMR spectroscopy. Both quantitative ssNMR approaches detect the decay of ^{13}C signals from isotope-labeled sites due to the reintroduction of ^{13}C - ^{13}C or ^{13}C - ^{31}P dipolar couplings, which are inversely proportional to the internuclear distances. A faster time-dependent evolution of ^{13}C signal intensities indicates stronger dipolar coupling and therefore corresponds to shorter internuclear distances. Combined with selectively single- ^{13}C isotope-labeled samples, these approaches mapped quantitative, time-dependent changes in $A\beta$ peptide chain assembly and membrane localization during the early stages of membrane-associated $A\beta$ aggregation. Additionally, our previous dynamic nuclear polarization (DNP)-enhanced ssNMR studies demonstrated significant signal enhancements in isotope-labeled $A\beta$ samples in the presence of excess natural abundance lipids, enabling the detection of molecular interactions through multidimensional NMR spectroscopy^{21,22}.

Results

$A\beta_{1-42}$ achieves enriched β -strand conformation and inter-strand proximities throughout the primary sequence before the onset of fibrillation

We first applied CD spectroscopy (spectra shown in Supplementary Fig. S2) and ThT fluorescence spectroscopy to determine the timeframe of the nucleation phase in the membrane-associated $A\beta$ fibrillation process. As shown in Fig. 1A, both $A\beta_{1-40}$ and $A\beta_{1-42}$ exhibited typical nucleation-driven aggregation processes with sigmoidal ThT kinetics. Fitting these data yielded t_{lag} values of 20.0 ± 1.5 h for $10 \mu\text{M}$ $A\beta_{1-40}$ and 10.5 ± 2.2 h for $5 \mu\text{M}$ $A\beta_{1-42}$. Notably, $A\beta_{1-42}$ exhibited approximately two-fold faster fibrillation kinetics at half the concentration of $A\beta_{1-40}$, consistent with our previous finding that $A\beta_{1-42}$ nucleates first in mixtures containing three times the amount of $A\beta_{1-40}$. The time-dependent changes in CD intensity at 218 nm, typically assigned to the β -strand conformation, revealed an earlier onset of the β -strand secondary structure compared to fibril elongation. The best-fit half-time of CD signal for $10 \mu\text{M}$ $A\beta_{1-40}$ and $5 \mu\text{M}$ $A\beta_{1-42}$ was 15.7 h and 2.1 h, respectively.

To understand the molecular-level structural changes of $A\beta_{1-42}$ during nucleation and its differences from $A\beta_{1-40}$, we applied ^{13}C -PITHIRDS-CT spectroscopy¹⁹ to singly ^{13}C -labeled samples (see Supplementary Table S1 for a list of samples and ssNMR experiments), with incubation times ranging from 3 to 15 h. Representative ^{13}C -PITHIRDS-CT spectra with 3- and 15-h incubation were shown in Fig. 1B (with additional spectra provided in Supplementary Fig. S3). Quantitative analysis took into account the natural abundance of lipid carbons that overlapped with the ^{13}C chemical shifts with C', Ca, or C β . The actual fractions of membrane-bound $A\beta_{1-42}$ at various incubation times were determined by the bicinchoninic acid (BCA) assay (Supplementary Fig. S4). The corrected ^{13}C -PITHIRDS-CT decay curves (Fig. 1C) were fit to derive the average ^{13}C - ^{13}C distances (Table 1 and Fig. 1D) using the SIMPSON simulation package²³.

In general, the ^{13}C -PITHIRDS results clearly demonstrated the time-dependent formation of parallel- β -sheet structures, as indicated by more rapid decay curves with longer incubation times. Before the onset of fibrillar elongation (i.e., at 3, 6, and 9 h of incubation), all tested residues in $A\beta_{1-42}$ showed significant inter-strand proximity. The most significant parallel- β -sheet structural convergence occurred between 6 and 9 h of incubation, where the inter-strand distances at N-terminal residues such as A2, F4, and V12 decreased from $>8.5 \text{ \AA}$ to 5.5 – 6.0 \AA . This timescale was consistent with the CD and ThT results, which showed the maturation of the secondary β -strand conformation and the onset of fibrillation between 6 and 9 h. In comparison, we previously showed that only residues G25, G29, L34, and V36 in membrane-associated $A\beta_{1-40}$ with 15-h incubation had inter-strand distances ranging from 6.0 to 6.5 \AA ²⁰. Residues closer to the N-terminus, such as F19 and A21, remained farther apart with interstrand distances longer than 8.0 \AA . Thus, structural convergence during the nucleation phase is significantly accelerated throughout the entire primary sequence in $A\beta_{1-42}$ compared to $A\beta_{1-40}$.

The nucleation of $A\beta_{1-42}$ modulates membrane fluidity and phospholipid dynamics, driven by membrane-surface-embedded oligomers

Compared to $A\beta_{1-40}$, $A\beta_{1-42}$ induced more significant local membrane disruptions, as evidenced by shortened lag periods and higher levels of leakage (Supplementary Fig. S5). Since the $A\beta$ peptides were added exogenously to liposomes, we anticipated that the physicochemical properties of phospholipid headgroups would be modulated during the membrane-associated nucleation process. Figure 2A shows the time-dependent changes of Laurdan fluorescence general polarization (GP) upon incubation with $A\beta$, a measurement of membrane fluidity²⁴. An increase in GP was induced by the nucleation and fibrillation of $A\beta_{1-42}$, but not $A\beta_{1-40}$, correlating with the stronger membrane-modulation effects of $A\beta_{1-42}$. Similar increase of Laurdan fluorescence GP was observed in cholesterol-inserted model membranes, indicating the increase of hydrophobic interactions²⁰. Modulation of microscopic phospholipid dynamics by $A\beta_{1-42}$ was further assessed by ^{31}P relaxation spectroscopy (Supplementary Figs. S6 and S7 for representative ^{31}P spectra and decay curves). Quantitative analysis of ^{31}P T_1 and T_2 relaxation rates provided correlation times for the microsecond timescale lateral diffusive motion (Fig. 2B) and the nanosecond timescale uniaxial rotational/wobbling motion (Fig. 2C) of lipids^{12,25,26}. A general decrease trend in these correlation times (Supplementary Table S2) as a function of incubation time implied an increase of local phospholipid dynamics due to membrane-associated nucleation of $A\beta_{1-42}$. Temperature-dependent changes in correlation times revealed decreases in activation energies for both motions (Supplementary Fig. S8). The modulations of phospholipid dynamics agreed with the enhancement of membrane content leakage observed for $A\beta_{1-42}$, indicating the induction of local defects by the aggregation process²⁷.

To understand how the $A\beta_{1-42}$ -lipid interaction proceeds during the nucleation process of membrane-associated $A\beta_{1-42}$ fibrillation, we performed ^{13}C - ^{31}P REDOR spectroscopy²⁸ (Fig. 3A and Supplementary Fig. S9) to probe residue-specific proximities to lipid headgroups. Experiments were conducted under the same conditions as those for the

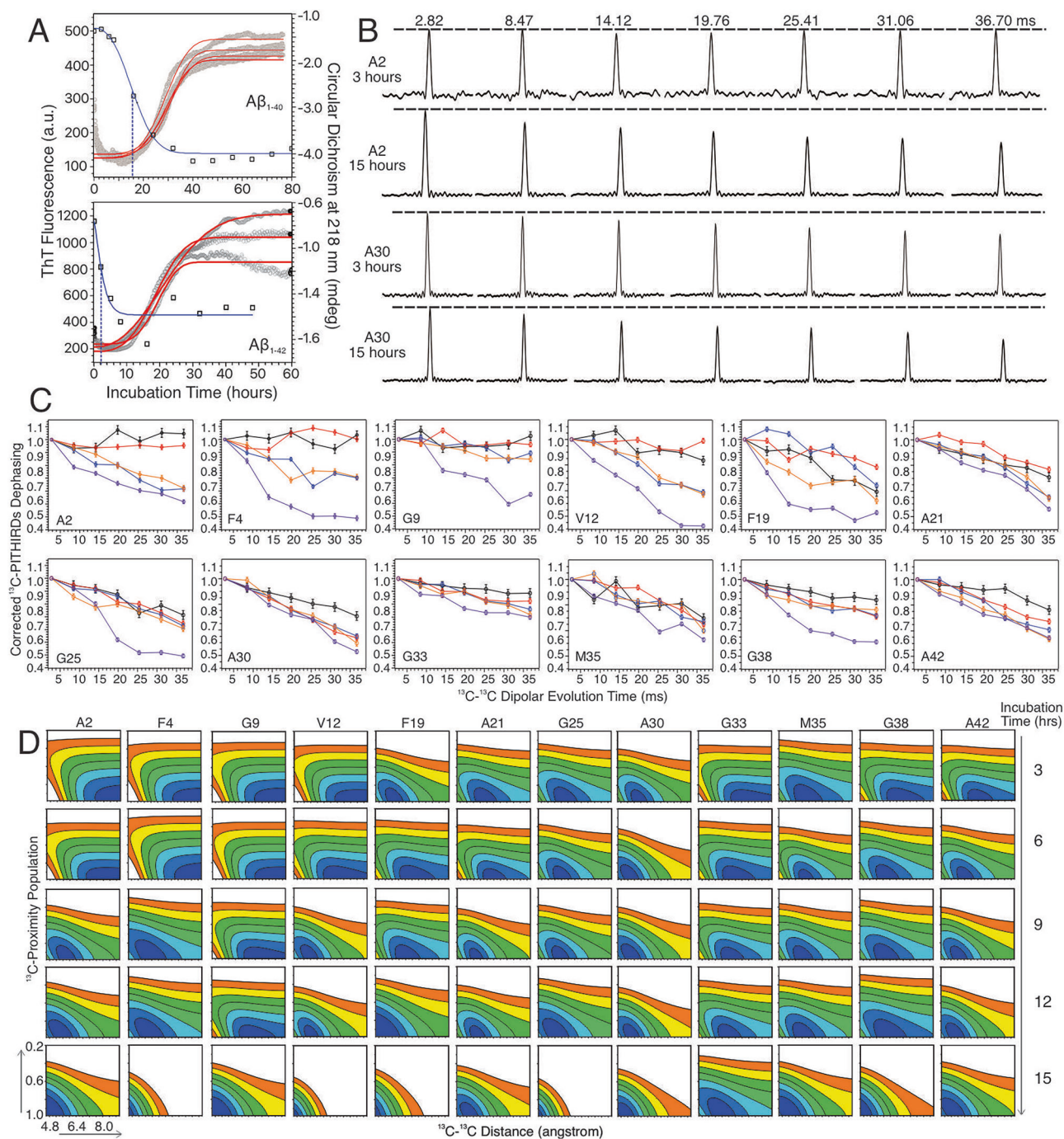


Fig. 1 | Characterization of the membrane-associated $A\beta_{1-42}$ assembling. **A** ThT fluorescence (left y-axis) and CD intensity at 218 nm (right y-axis) along the incubation of membrane-associated $A\beta_{1-40}$ (10 μ M, top) and $A\beta_{1-42}$ (5 μ M, bottom). Red curves show sigmoidal fitting of ThT kinetics to the equation $I_t = I_0 + (I_\infty - I_0) [1 - \exp(-(kt)^n)]$, from which the lag periods were derived. The blue curves and dashed lines show the same sigmoidal fitting for the time-dependent CD intensities and the derived $t_{1/2}$ values, where $I_t - I_0 \equiv \frac{1}{2}(I_\infty - I_0)$. **B** Representative ^{13}C -PITHIRDS-CT spectra for residues A2 and A30 with 3- and 15-h incubation in POPC liposomes. ^{13}C - ^{13}C dipolar evolution times were given on top of the spectra.

C Plots of corrected residue-specific ^{13}C -PITHIRDS-CT dephasing curves (see S.I. for the natural abundance correction) at different incubation times. Color-coding: black, 3 h; red, 6 h; blue, 9 h; orange, 12 h; purple, 15 h. Error bars represent the signal-to-noise levels of individual sets of ^{13}C -PITHIRDS-CT spectra. **D** Contour plots for the fitting of ^{13}C -PITHIRDS-CT dephasing results using SIMPSON (details provided in S.I.). Contour levels show 1-7 times of $\sigma \equiv \sqrt{2(N-n)}$ around χ_{\min}^2 , where N is the number of data points ($N = 7$) and n is number of fitting parameters ($n = 2$).

^{13}C -PITHIRDS-CT, allowing us to track the time-dependent changes in $A\beta_{1-42}$ assembly and membrane location simultaneously. Plots of REDOR dephasing (i.e., $\Delta S/S_0 \equiv (S_0 - S_1)/S_0$, Fig. 3B; see Supplementary Methods for details of quantitative analysis) were fitted to derive the average ^{13}C - ^{31}P distances and lipid-phosphate-proximity ^{13}C populations (Fig. 3C and Supplementary Table S3). Most of the fittings yielded similarly correlated χ^2

value patterns as functions of the two variables (i.e., ^{13}C - ^{31}P distances and lipid-phosphate-proximity ^{13}C populations), suggesting that for individual residues, it is the time-dependent trend, rather than the best-fit distances or populations values, that was validated. A few samples showed well-defined minimum χ^2 ranges, especially for the samples with 12-h incubation time (Table S3). Several residues, such as G9, A21, A30, and G33, are located in

Table 1 | Best-fit residue-specific ^{13}C - ^{13}C distances (in Å) for intermediate membrane-associated $\text{A}\beta_{1-42}$ assembly^a

Incubation times (h)	A2	F4	G9	V12	F19	A21	G25	A30	G33	M35	G38	A42
3	>9.0	>9.0	>9.0	8.6 (1.6)	5.8 (0.8)	6.2 (0.8)	6.2 (0.8)	6.0 (0.6)	7.4 (1.2)	6.2 (0.8)	7.0 (1.4)	6.8 (1.0)
6	8.4 (1.6)	>9.0	>9.0	7.2 (1.0)	6.8 (1.0)	6.8 (1.0)	6.0 (0.8)	5.4 (0.8)	6.8 (1.0)	6.2 (0.6)	6.2 (1.0)	6.0 (0.8)
9	5.6 (0.8)	6.0 (1.2)	7.4 (1.0)	5.6 (0.8)	6.4 (1.0)	5.8 (0.8)	6.0 (0.8)	5.6 (0.6)	6.6 (1.0)	6.0 (0.6)	6.2 (0.8)	5.8 (0.6)
12	5.8 (0.8)	6.0 (1.0)	7.0 (0.8)	5.6 (0.8)	5.4 (0.8)	5.8 (0.8)	5.8 (0.8)	5.4 (0.6)	6.4 (0.8)	6.0 (0.6)	6.2 (0.8)	5.6 (0.6)
15	4.8 ^b	4.8	5.2 (0.8)	4.8	4.8	5.4 (0.8)	4.8	5.2 (0.4)	6.0 (0.8)	5.4 (0.6)	5.0 (0.4)	5.2 (0.4)

^aOnly the best-fit ^{13}C - ^{13}C distances are reported. The ^{13}C -proximity populations are not included in the table but shown in Fig. 1D.

^bThe lower threshold of ^{13}C - ^{13}C distance was set to 4.8 Å in the fitting.

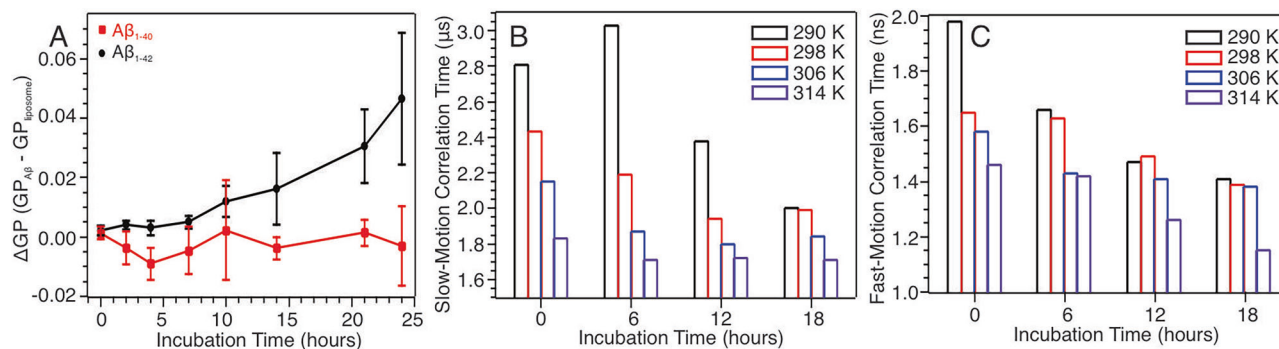


Fig. 2 | Characterization of the phospholipid dynamics of bilayers. **A** Plot of the change of Laurdan fluorescence general polarization of POPC liposomes upon incubation of 10 μM $\text{A}\beta_{1-40}$ and 5 μM $\text{A}\beta_{1-42}$. Error bars represent standard

deviation from three repetitions ($n = 3$). Plots of microsecond timescale (**B**) and nanosecond timescale (**C**) correlation times derived from the ^{31}P T_1 and T_2 relaxation spectroscopy.

proximity with lipid phosphates with ~ 5 Å ^{13}C - ^{31}P distances. Interestingly, a global best-fit lipid-phosphate-proximity population of ~ 0.3 was obtained, suggesting that about one-third of the membrane-bound $\text{A}\beta_{1-42}$ located close to lipids at this incubation time.

Combined with the ^{13}C -PITHIRDS-CT results, the interpretation of the intermediate states is summarized schematically in Fig. 4. The time-dependent behavior of individual residues is presented in three color-coded columns: (1) The greyscale (left, Fig. 4) shows the convergence to parallel- β -sheet assemblies. All residues exhibited shorter inter-strand distances at longer incubation times, but with residue-specific rates of structural convergence. The segment F19-A30, as well as discrete regions around M35 and the C-terminus, reached shorter average inter-strand distances earlier in the nucleation process compared to other parts of the $\text{A}\beta_{1-42}$ sequence. Interestingly, residues F19 and A21 showed a unique trend, with longer interim inter-strand distances at 6 h. These observations suggest that shorter segments from the middle to the C-terminus of $\text{A}\beta_{1-42}$ primary sequence may form discrete nucleation sites, and transient registry shift could occur within segments like F19-A21. Out-of-registry β -sheets and antiparallel β -sheets structures have been reported in $\text{A}\beta$ oligomers and protofibrils, and these structures are typically associated with higher level of cytotoxicity compared to mature parallel-in-register β -sheet fibrils²⁹⁻³¹. (2) The red and blue scales (middle and right, Fig. 4) represent residue-specific lipid-phosphate proximity. Several residues, including G9, F19, A21, G25, A30, G33 and G38, exhibited a consistent decrease in lipid-phosphate-proximity populations. Some of these residues, such as A30 (~ 5.0 – 7.0 Å), A21 (~ 5.5 – 7.5 Å), G9 (~ 5.0 – 7.0 Å), and G38 (5.0 – 7.5 Å), maintained relatively fixed ^{13}C - ^{31}P distance range, indicating their proximity to lipid headgroups throughout the nucleation phase. As the β -sheet structures grew, their lipid-phosphate-proximity population decreased because of the shielding of effective ^{13}C from lipids. (3) A few residues, such as F4, V12 and M35, remained distant from lipid headgroups throughout nucleation. Other residues, especially the N-terminal A2 and C-terminal A42, consistently stayed close to lipid ^{31}P . Given the broad distribution of ^{31}P -proximity residues across the entire $\text{A}\beta_{1-42}$ sequence, it is reasonable to conclude that the peptide adopts a surface-embedded position during nucleation. A recent all-atom MD

simulation investigated the early-stage membrane interactions of $\text{A}\beta_{1-42}$ dimers³², which revealed that residues with strong lipid headgroup interactions were primarily located at the N-terminus and from F20 to A30. This latter segment aligns well with the current ^{13}C - ^{31}P REDOR results. While the MD simulation suggested that N-terminal interactions may involve more specific interactions with PE and PS lipids, which are absent in the present membrane bilayer model, the current REDOR data still show proximity at A2, consistent with the strong interactions observed between D1 and PC lipids in the simulation.

DNP-ssNMR results demonstrate molecular-level structural convergence during the membrane-associated nucleation of $\text{A}\beta_{1-42}$

DNP-ssNMR spectroscopy has proven effective in providing detailed information about molecular structures and interactions during the $\text{A}\beta$ fibrillation process^{21,33-35}. In this study, membrane-bound $\text{A}\beta_{1-42}$ was collected at various incubation times, and the membrane-permeative bi-radical AsymPol-POK^{36,37} was added to the hydrated membrane- $\text{A}\beta_{1-42}$ pellets. The samples typically contained 0.4–0.7 mg of isotope-labeled $\text{A}\beta_{1-42}$ aggregates, diluted by a 100–150 molar excess of phospholipids. DNP application at 14.1 T/600 MHz yielded between 24 and 52-fold signal enhancements, characterized as the intensity ratio between NMR spectra acquired with and without microwave irradiation ($\epsilon_{\text{on}}/\epsilon_{\text{off}}$), depending on the sample incubation time and spectral frequency range (Supplementary Fig. S10). The nuclear hyperpolarization buildup times range from 1.2 and 3.0 s.

Two-dimensional (2D) ^{13}C - ^{13}C DARR spectra with 25 ms (Supplementary Fig. S11) and 250 ms mixing times (Fig. 5A) were collected to investigate the time-dependent structural convergence of membrane-bound $\text{A}\beta_{1-42}$. At short incubation times (e.g., one and 2 h), most intra-residue cross peaks, including the backbone C'/Ca and Ca/C β cross peaks, were poorly resolved. Only G38, a residue near the C-terminus of $\text{A}\beta_{1-42}$, exhibited a relatively strong C'/Ca cross peak (representative 1D slices are shown in Fig. 5B). After 6 h of incubation, intra-residue cross peak intensities were significantly increased, and certain inter-residue cross peaks, such as F19-I32 and/or F19-L34, began to emerge. These inter-residue contacts,

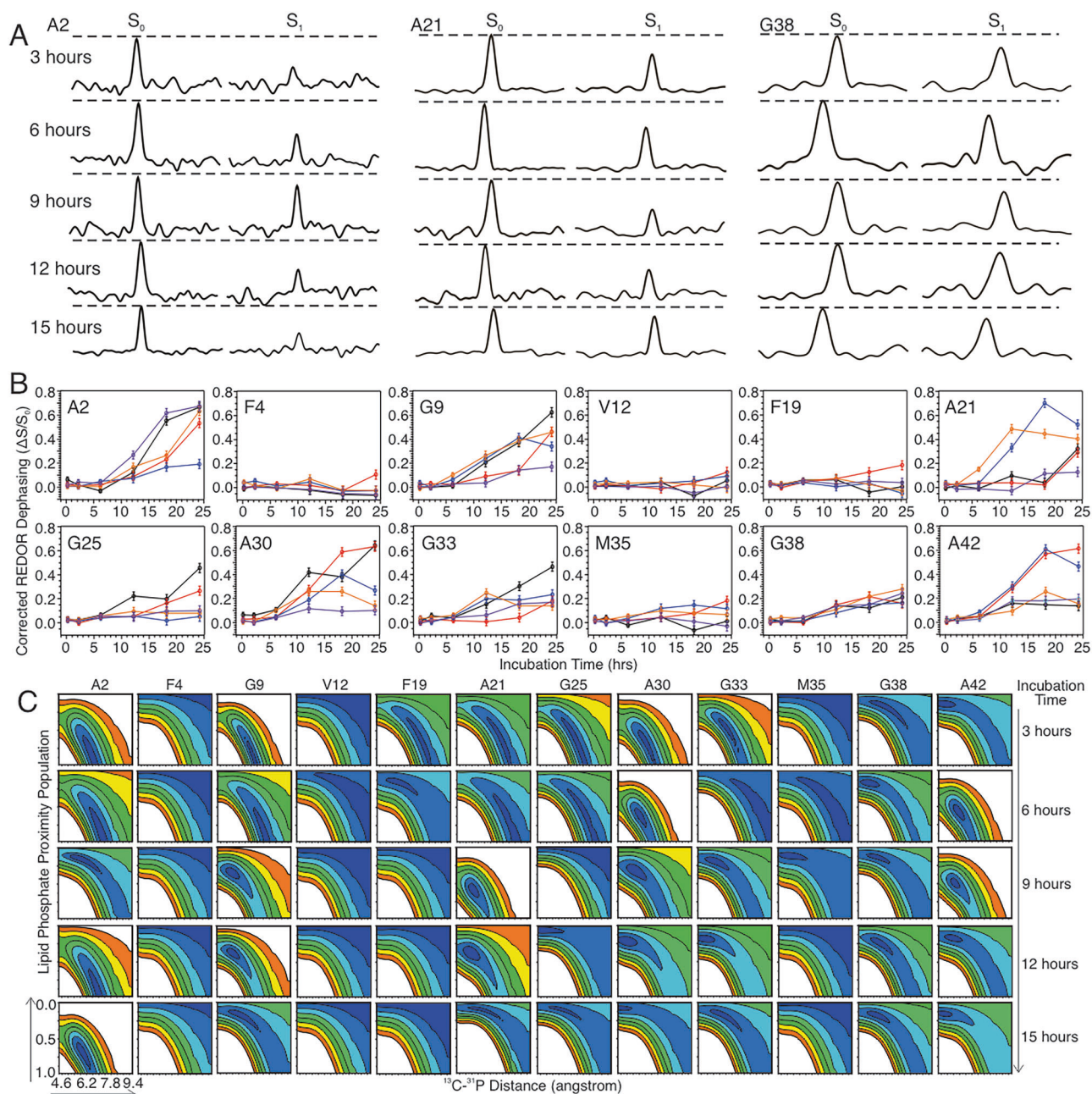


Fig. 3 | Characterization of the membrane lipid proximity to A β ₁₋₄₂.

A Representative ^{13}C - ^{31}P REDOR spectra for residues A2, A21, and G38 with 3–15 h' incubation in POC liposomes and 24.1 ms ^{13}C - ^{31}P dipolar evolution time.

Horizontal dashed lines highlight the differences between S_0 and S_1 spectra. **B** Plots of corrected residue-specific ^{13}C - ^{31}P REDOR dephasing (dephasing $\equiv (S_0 - S_1)/S_0$, see *S.I.* for the natural abundance correction) at different incubation times. Color-

coding: black, 3 h; red, 6 h; blue, 9 h; orange, 12 h; purple, 15 h. Error bars represent the signal-to-noise levels of individual sets of ^{13}C - ^{31}P REDOR spectra. **C** Contour plots for the fitting of ^{13}C - ^{31}P REDOR dephasing results using SIMPSON (details provided in *S.I.*). Contour levels show 1–7 times of $\sigma \equiv \sqrt{2(N-n)}$ around χ_{\min}^2 , where N is the number of data points ($N = 6$) and n is number of fitting parameters ($n = 2$).

which have been reported in several previous A β ₁₋₄₂ fibril structures as part of the fibrillar cores^{38–40}, suggest that specific tertiary structural domains may already be forming during the early stages of nucleation. Structural convergence continued with further incubation at 9 and 15 h, where a dominant set of cross peaks appeared for most residues. Notably, the N-terminal E3 also showed a predominant set of intra-residue cross peaks, indicating that the entire A β ₁₋₄₂ peptide had adopted a rigid and structured conformation at this stage. This observation is consistent with the ^{13}C -PITHIRDS results, where residues A2 and F4 exhibited parallel- β -sheet structural features at 15 h. The structural convergence of membrane-associated A β ₁₋₄₂ was further confirmed by 2D DQ-SQ correlation spectra (Fig. 5C), where well-defined intra-residue cross peaks were observed only after 9 h of incubation.

Lastly, we observed cross peaks between the aromatic ^{13}C sites in F19 and the natural abundance lipid aliphatic ^{13}C sites (i.e., ~31–33.5 ppm, corresponding to the most abundant lipid carbons C4–C13). Interestingly, these cross peaks exhibited higher intensities at shorter incubation times (e.g., 1–6 h) but diminished afterward, showing an opposite trend compared to the inter-residue cross peaks between F19 and I32/L34. This observation suggests that the aromatic side chain of F19 was initially exposed to the hydrophobic interior of the bilayer and later incorporated into the formation of early-stage tertiary structural domains in fibrillar core. Additionally, F19 likely inserted into the outer leaflet of the bilayer, which is consistent with the ^{13}C - ^{31}P REDOR results, where F19 was found to

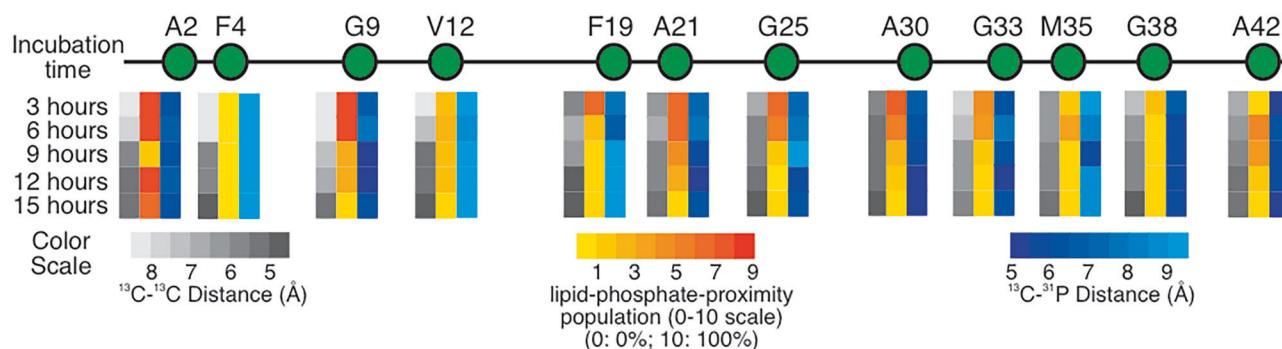


Fig. 4 | Color-scale presentation of the time-dependent and residue-specific $A\beta_{1-42}$ chain assembly and lipid headgroup proximity. Color scales are derived from quantitative fitting of ^{13}C -PITHIRDS-CT and ^{13}C - ^{31}P REDOR results described in previous sections.

be far from the phospholipid headgroups. Similar membrane positioning and hydrophobic interactions involving F19 were observed in a previous all-atom MD simulation¹⁸.

Discussion

Molecular-level structural convergence along the membrane-associated $A\beta_{1-42}$ nucleation process

Multiple sets of biophysical and structural characterizations were conducted in the current study to systematically map the intermediate states of membrane-associated $A\beta_{1-42}$ throughout the fibrillation process. Fitting the sigmoidal ThT kinetics curves revealed three characteristic phases at the early stages of nucleation and fibrillation: (1) A “silence phase” where the ThT fluorescence intensity remains unchanged up to ~8 h, suggesting the absence of parallel- β -sheet-like stacking constructs in $A\beta_{1-42}$; (2) A “transition phase” between 9 and 12 h, during which the increase of ThT fluorescence indicates a transition towards fibrillar elongation; (3) The ThT kinetics then exhibit an exponential increase, signifying the typical “elongation phase”. By combining ^{13}C -PITHIRDS-CT, ^{13}C - ^{31}P REDOR, and 2D DNP-ssNMR spectroscopy, we examined the molecular-level and residue-specific details of the structures and lipid interactions of $A\beta_{1-42}$ intermediates across these three phases.

As illustrated in Fig. 6, significant molecular-level structural transitions have already emerged during the “silence phase”. First, membrane-associated $A\beta_{1-42}$ achieves secondary structural convergence, supported by the development of negative ellipticity at 218 nm in CD spectroscopy and the amplification of predominant intra-residue cross peaks in DNP-ssNMR from 1 to 6 h. Second, segments within F19-A30 and M35-A42 show close inter-strand distances, though parallel- β -sheets have not yet formed. These segments represent the typical hydrophobic cores in mature $A\beta_{1-42}$ fibrillar structures^{41–44}. In the meanwhile, certain tertiary contacts, such as F19-I32/L34, start to form, which also imply the assembly of early fibrillar core. A recent ssNMR study captured the early-stage $A\beta_{1-40}$ intermediate states using rapid mixing and freezing techniques, reporting a similar time-dependent increase in the cross-peak volumes, which indicates stronger intra- and inter-residue interactions³⁴. We observed that individual residues within these segments showed distinct time-dependent assembling trends. For instance, a transient increase of inter-strand distances was observed for residues F19 and A21. In addition, most glycine residues (e.g., G33 and G38) exhibited a slower assembling rate compared to other sites. These results suggest that the formation of parallel- β -sheet occurs at discrete short pieces within the F19 to C-terminal segment.

During the “transition phase”, a predominant set of intra-residue cross peaks (i.e., secondary structure) matures, and the inter-strand distances decrease further to 5–7 Å across the $A\beta_{1-42}$ sequence. At this stage, the most significant structural convergence occurs at the N-terminal segment of $A\beta_{1-42}$, including residues A2, F4, and V12. This indicates the formation of a rigid, fibrillation-prone nucleus. Highly ordered N-terminal segments were shown to stabilize the tertiary and/or quaternary interfaces of $A\beta_{1-42}$ fibrillar cores. Additionally, the lipid-phosphate-proximity population for residues F19-A30 shows a decrease trend between 6 and 9 h, suggesting the initiation

of parallel- β -sheet-like assemblies, during which most ^{13}C sites are incorporated into larger β -sheet-like plaques and shielded from lipids. By 15 h, when the ThT kinetics enter the “elongation phase”, no further changes are observed in the secondary structure of $A\beta_{1-42}$. However, the inter-strand distances and lipid-phosphate-proximity populations further decrease, highlighting the maturation of parallel- β -sheet structures.

The molecular basis of different membrane-disrupting properties between $A\beta_{1-42}$ and $A\beta_{1-40}$

Compared to the abundant $A\beta_{1-40}$ in the human brain, the more pathological $A\beta_{1-42}$ is known to be more aggregation-prone and to induce greater cellular toxicity at lower concentrations^{45,46}. Co-incubation of $A\beta_{1-40}$ and $A\beta_{1-42}$ at the physiological molar ratio (i.e., ~3:1) exhibited multi-stage fibrillation features, both in the presence and absence of membrane-mimicked liposomes, with the initial aggregation originating from the lower-abundance $A\beta_{1-42}$ ^{22,47}. Recent cryogenic electron tomography (Cryo-ET) studies indicated that both $A\beta_{1-40}$ and $A\beta_{1-42}$ induced significant membrane curvature changes and local defects within membrane leaflets in their oligomeric states, but not in their monomeric forms^{27,48}. However, few pronounced differences between $A\beta_{1-40}$ and $A\beta_{1-42}$ were observed. Therefore, from a membrane disruption perspective, it remains unclear whether and how the differences in their aggregation properties correlate with their varying cellular toxicity levels.

Our results provide insights into the molecular basis for the differing membrane-disruptive effects of $A\beta_{1-42}$ and $A\beta_{1-40}$, with $A\beta_{1-42}$ inducing more significant content leakage and membrane fluidity modulation. A recent single molecular fluorescence spectroscopy study also showed different membrane insertion abilities of $A\beta_{1-42}$ and $A\beta_{1-40}$ might correlate with their distinct cytotoxicity levels⁴⁹. We previously characterized the residue-specific inter-strand distances and lipid-phosphate-proximity populations in membrane-associated $A\beta_{1-40}$ at 5 and 15-h incubation times²⁰. Given the ThT-based lag period of ~20 h, these time points correspond to the first phase of fibrillation in $A\beta_{1-40}$, analogous to the 1–6-h time points for $A\beta_{1-42}$. Three major differences between $A\beta_{1-42}$ and $A\beta_{1-40}$ were observed: First, $A\beta_{1-42}$ adopts closer inter-strand distances, indicating tighter β -sheet-like assemblies compared to $A\beta_{1-40}$. At the residue-specific level, F19, A21, G25, A30, and M35 in $A\beta_{1-42}$ all showed inter-strand distances of 5–6 Å, and G33 showed 6–7 Å. In contrast, in $A\beta_{1-40}$, F19, A21, and A30 remained at 7.5–8 Å. This trend of tighter packing at early stages was extended to the C-terminal residues G38 and A42, suggesting that the entire C-terminal half of $A\beta_{1-42}$ (e.g., F19-A42) tends to assemble more rapidly. For $A\beta_{1-40}$, however, the initial assembly is likely limited to the shorter segments within the C-terminal and/or loop domains (e.g., G25-G29 and around L34).

Second, the lipid-phosphate-proximity populations at the early stage for $A\beta_{1-42}$ were significantly higher compared to $A\beta_{1-40}$. For example, residues A2, G9, A21, G25, and A30 in $A\beta_{1-42}$ all exhibited > 50% ^{31}P -proximity populations at the 3–6-h incubation stage, while the maximum lipid-phosphate-proximity population for any probed residue in $A\beta_{1-40}$ was less than 10%. This result suggests that low-order $A\beta_{1-42}$ oligomers, which form rapidly and possess well-defined parallel- β -sheet-like structures in the F19-

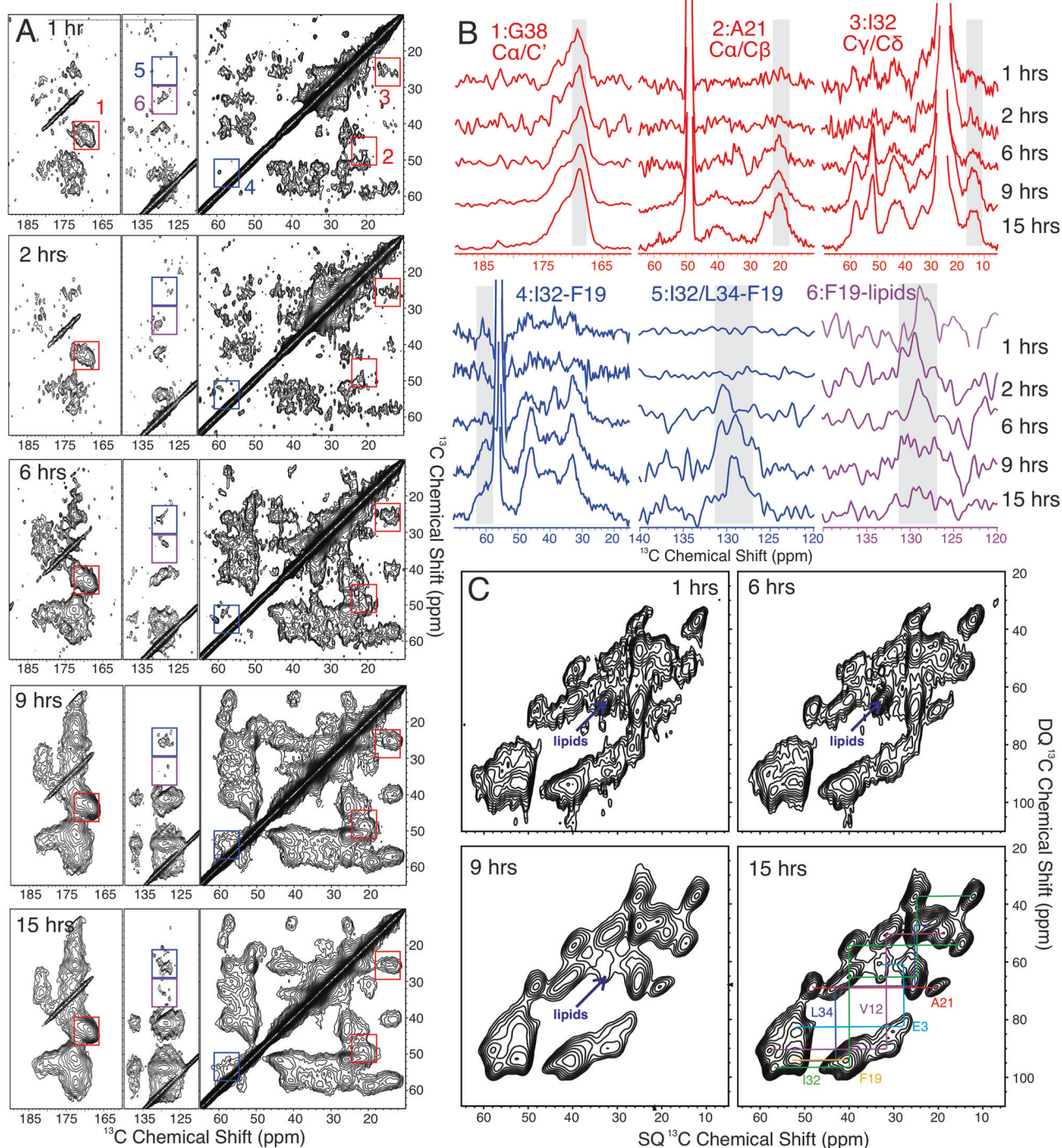


Fig. 5 | DNP-ssNMR spectra of the $A\beta_{1-42}$ -membrane samples at intermediate incubation times in POPC liposomes. All ssNMR samples contain selective- ^{13}C isotope labeling at residues E3, V12, F19, A21, I32, L34 and G38. **A** 2D ^{13}C - ^{13}C DARR spectra with 250 ms mixing time. Colored rectangles highlight the spectral regions from which the 1D slides are extracted. **B** 1D slides that represent the ^{13}C chemical shifts in the t1 dimension of the rectangle regions. Color-coding for panels (A, B):

red, intra-residue cross peaks; blue, inter-residue cross peaks; purple, cross peaks between ^{13}C -sites in $A\beta_{1-42}$ and natural abundance ^{13}C s in lipids. **C** 2D DQ-SQ correlation spectra acquired on the same samples as for the DARR spectra. Colored lines in the 15-h spectrum highlight the intra-residue aliphatic cross peaks for individual labeled residues. All spectra were processed with 50 Hz Gaussian line broadening in each dimension.

A42 domain, dominate the interactions with membranes at the nucleation stage. It has been shown previously that $A\beta_{1-42}$ is more likely to form stable small oligomers (e.g., trimer, pentamer, hexamer, etc.) in solution, which act as effective nucleation species^{50–52}. The size of these proposed oligomers is consistent with the lipid-phosphate-proximity populations, where about one-half to one-third of the isotope-labeled ^{13}C sites locate close to ^{31}P between 9 and 12 h. Similar oligomers may form rapidly in the membrane environment and directly contribute to membrane disruption.

Third, the same region in the $A\beta_{1-42}$ primary sequence, likely within the F19-A30 segment, initiates both the interstrand assembly and membrane-disruptive interactions. This is supported by the combination of ^{13}C -PITHIRDS-CT and ^{13}C - ^{31}P REDOR results (Fig. 4), where residues F19, A21, G25, and A30 exhibited both close inter-strand distances and high lipid-phosphate-proximity populations at the 3–6-h incubation stage. This contrasts our previous findings for $A\beta_{1-40}$, where residues with high lipid-phosphate-proximity populations (e.g., F19, A21, and G25) and those with

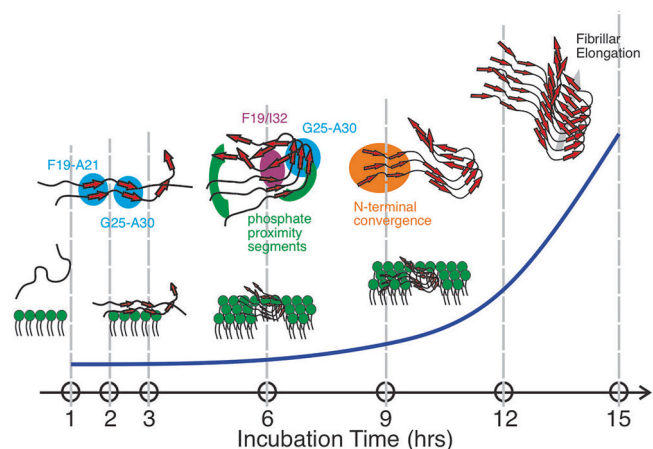


Fig. 6 | Schematic presentation of the membrane-associated $A\beta_{1-42}$ intermediate states. The blue curve indicates a typical ThT fluorescence build-up trace. Red arrows indicate the segments that adopt the β -strand conformation. Cyan, purple, and orange circles highlight the assemblies of β -sheets, tertiary contacts, and N-terminal domains, respectively.

close inter-strand distances (e.g., G25, G29, L34, and V36) were separated²⁰. We hypothesize that in $A\beta_{1-42}$, this overlapping between inter-strand packing and membrane interaction leads to competition between peptide chain assembly and membrane insertion, which may stabilize the rapidly forming low-order oligomers that can more efficiently insert into the bilayer. For $A\beta_{1-40}$, on the contrast, the binding of peptides and the initial interstrand assembling may occur in different primary sequence regions, which allows the formation of larger exterior $A\beta$ assemblies with less membrane-disruptive effects. These differences may explain the higher levels of content leakage and membrane fluidity changes observed with $A\beta_{1-42}$ compared to $A\beta_{1-40}$.

Conclusions

The present ssNMR studies provide a molecular-level understanding of the membrane-associated nucleation process of $A\beta_{1-42}$. Through quantitative analysis of intermediate-state samples with selective isotope labeling, we demonstrate that surface-embedded, low-order $A\beta_{1-42}$ oligomers strongly interact with the phospholipid headgroups of membranes during nucleation towards fibril formation. Compared to the less pathological $A\beta_{1-40}$, the membrane-interactive $A\beta_{1-42}$ shows closer proximity to lipid headgroups, broader lipid-contacting segments, and lower oligomer states, which may allow for more effective insertion into bilayers. These differences correlate positively with the higher levels of membrane-disruptive effects and cytotoxicity exhibited by $A\beta_{1-42}$. Future studies may also involve mixture of $A\beta_{1-40}$ and $A\beta_{1-42}$ in more biologically relevant membrane-mimicked model systems. Additionally, residues that undergo structural transitions and converge at various stages of membrane-associated nucleation are identified. This information may assist in the future design of agents targeting these early-stage intermediates.

Methods

Peptide synthesis and purification

All $A\beta$ peptides ($A\beta_{1-40}$ $m/z = 4329.8$ Da; $A\beta_{1-42}$ $m/z = 4514.1$ Da) were synthesized using a microwave-assisted peptide synthesizer (Biotage Initiator+ Alstra™) following standard Fmoc-based solid-phase peptide synthesis protocols. The crude peptides were purified by HPLC (Agilent 1260 Infinity) employing a reversed-phase C18 column, and the products were verified by LC-MS to >95% purity (Shimadzu LCMS 2020, see Supplementary Fig. S1). Detailed synthesis and purification conditions are provided in the Supporting Information.

Liposome preparation and exogenous addition of $A\beta$

Liposomes were prepared following a standard protocol established in our previous studies^{10,20,53,54}. Briefly, the desired phospholipids were dissolved in

chloroform, which was then removed by gentle N_2 flow, followed by the formation of lipid films under vacuum for at least 8 h. The dried lipid film was resuspended in 10 mM phosphate buffer (pH 7.4, containing 0.01% NaN_3) and subjected to 10 freeze-thaw cycles, alternating between liquid N_2 and 50–60 °C water bath. The resuspended liposomes were extruded through 100 nm (for Thioflavin-T fluorescence and circular dichroism spectroscopy), 200 nm (for Laurdan fluorescence assay), or 400 nm (for ssNMR measurements) pore-size membrane filters (using a mini-extruder set from Avanti Polar Lipids, Inc.). Liposome solutions were freshly prepared before use. For all experiments, except for the calcein leakage assay, a single-component liposome containing only 1-palmitoyl-2-oleoyl-glycerol-3-phosphocholine (POPC, Avanti Polar Lipids Inc.) was utilized. For the calcein leakage assay, liposomes were prepared with the following three compositions: POPC only, POPC and 1-palmitoyl-2-oleoyl-glycerol-3-phosphoethylethylamine (POPE) in a 3:1 molar ratio, and POPC, POPE, and 1-palmitoyl-2-oleoyl-glycerol-3-phosphoserine (POPS) in a 3:1:1 ratio.

Lyophilized $A\beta$ peptides were dissolved in hexafluoro-isopropanol (HFIP, Sigma Aldrich Inc.) at a concentration of 2 mg/mL. The solution was bath-sonicated for 1 min, followed by overnight incubation at room temperature to ensure complete dissolution. HFIP was then removed by gentle N_2 , and the sample was dried under vacuum for at least 8 h. The peptide film was dissolved in dimethyl sulfoxide (DMSO, Sigma Aldrich Inc.), and the concentration was determined using a nanodrop UV-VIS spectrometer (Thermo Scientific Inc.) at 280 nm, based on a molar extinction coefficient of $1420 M^{-1} cm^{-1}$ for both $A\beta_{1-40}$ and $A\beta_{1-42}$. For all samples, the $A\beta$ -DMSO stock was diluted into liposome solution to reach the final peptide concentration of 10 μM for $A\beta_{1-40}$ and 5 μM for $A\beta_{1-42}$, with a 1:30 $A\beta$ to total lipids molar ratio for $A\beta_{1-40}$ and 1:90 molar ratio for $A\beta_{1-42}$.

Biophysical Characterizations of $A\beta$ Aggregation and $A\beta$ -Membrane Interactions

The present work employed a combination of thioflavin-T (ThT) fluorescence assay, circular dichroism (CD) spectroscopy, calcein leakage assay, and Laurdan fluorescence assay to characterize $A\beta$ aggregation and membrane interactions. All assays followed standard procedures for liposome preparation, exogenous addition of $A\beta$ peptides, and incubation. Most assays used a simplified liposome model consisting of POPC. For the calcein leakage assay, three liposome models containing mixtures of POPC, POPE, and POPS were employed. Experimental details and associated data analysis for each assay are provided in the Supporting Information.

The ssNMR Spectroscopy

For ^{13}C -PITHIRDS-CT and ^{13}C - ^{31}P REDOR experiments, samples that contain $A\beta_{1-42}$ in POPC liposomes were incubated for the desired times and collected by ultracentrifugation on a Beckmann Coulter ultracentrifuge (Optima MAX-TL, 50,000 rpm for 30 min at 4 °C). The pellets were lyophilized, packed into a 2.5 mm magic angle spinning (MAS) rotor, and rehydrated using 1.0 $\mu L/mg$ deionized water. For ^{31}P relaxation spectroscopy, the pellets were packed directly into the 2.5 mm MAS rotors without lyophilization. For dynamic nuclear polarization (DNP) assisted ssNMR spectroscopy, samples were prepared by mixing the $A\beta_{1-42}$ -liposome pellets with a stock solution that contains 10 mM Asymopol-POK³⁶ in ^{13}C -depleted d_8 -glycerol/ D_2O/H_2O in a ratio of 60/30/10 vol%. Around 35 μL of the stock solution was directly added into the wet sample pellets; the mixture was vortexed vigorously for about 1 min⁵⁵ and transferred to a 3.2 mm sapphire rotor and closed with Vespel caps. The DNP-ssNMR rotors were frozen immediately and kept frozen before measurements.

Non-DNP ssNMR spectroscopy, including ^{13}C -PITHIRDS-CT, ^{13}C - ^{31}P REDOR, and ^{31}P relaxation experiments, was performed on a 600 MHz Bruker Avance III spectrometer equipped with a 2.5 mm Tri-Gamma HXY magic-angle spinning (MAS) probe tuned to $^1H/^{31}P/^{13}C$. PITHIRDS and REDOR experiments were conducted on rehydrated $A\beta$ -membrane pellets containing ~2 mg of selectively ^{13}C -labeled $A\beta$ aggregates and about 10 mg of lipids. The pulsed-spin locking (PSL) acquisition method⁵⁶ was applied to individual labeled sites to enhance spectral

sensitivity. The magic-angle spinning (MAS) frequencies were set to $20,000 \pm 2$ Hz and $10,000 \pm 2$ Hz, respectively, for PITHIRDS-CT and REDOR experiments. The For PITHIRDS-CT and REDOR, a complete set of ^{13}C spectra from a single labeled site (comprising eight and six dephasing time points, respectively) was collected over ~ 16 and ~ 24 h. The ^{31}P relaxation experiments were performed on fully hydrated A β -membrane pellets, with sample temperatures monitored via ^1H chemical shifts of H_2O . A full set of T_1/T_2 spectra at four different temperatures was acquired within 6 h.

MAS-DNP experiments were conducted at the National High Magnetic Field Laboratory (Tallahassee, USA) using a 600 MHz/395 GHz system, equipped with a Bruker NEO console and a 3.2 mm wide-bore MAS-DNP probe⁵⁷. For each sample, a ^1H - ^{13}C cross-polarization (CP) experiment was performed to assess sensitivity enhancement. Additionally, two 2D SQ-SQ DARR spectra with 25 ms and 250 ms mixing periods, along with a 2D DQ-SQ spectrum, were acquired within 8–15 h. Further details on the experimental setup, sample preparation, and quantitative data analysis procedures for ssNMR measurements are provided in the Supporting Information.

Data availability

The authors declare that all data supporting the findings of this study are available within the paper and its supplementary information files.

Received: 17 March 2025; Accepted: 23 April 2025;

Published online: 30 April 2025

References

- Altomare, D. et al. The probabilistic model of Alzheimer's disease: the amyloid hypothesis revised. *Nat. Rev. Neurosci.* **23**, 53–66 (2022).
- Cline, E. N., Bicca, M. A., Viola, K. L. & Klein, W. L. The amyloid- β oligomer hypothesis: beginning of the third decade. *J. Alzheimer Dis.* **64**, S567–S610 (2018).
- Rangachari, V., Dean, D. N., Rana, P., Vaidya, A. & Ghosh, P. Cause and consequence of A β - Lipid interactions in Alzheimer's disease pathogenesis. *Biochim. Biophys. Acta Biomembr.* **1860**, 1652–1662 (2018).
- Fabiani, C. & Antollini, S. S. Alzheimer's disease as a membrane disorder: spatial cross-talk among beta-amyloid peptides, nicotinic acetylcholine receptors and lipid rafts. *Front. Cell Neurosci.* **13**, 309 (2019).
- Ma, J. et al. Extracellular matrix proteins involved in Alzheimer's disease. *Chemistry* **26**, 12101–12110 (2020).
- Ke, P. C. et al. Implications of peptide assemblies in amyloid diseases. *Chem. Soc. Rev.* **46**, 6492–6531 (2017).
- Rawat, A., Langen, R. & Varkey, J. Membranes as modulators of amyloid protein misfolding and target of toxicity. *Biochim. Biophys. Acta Biomembr.* **1860**, 1863–1875 (2018).
- Andrade, S., Loureiro, J. A. & Pereira, M. C. The role of amyloid β -biomembrane interactions in the pathogenesis of Alzheimer's disease: insights from liposomes as membrane models. *Chemphyschem* **22**, 1547–1565 (2021).
- Bloom, G. S. Amyloid- β and tau: the trigger and bullet in Alzheimer's disease pathogenesis. *JAMA Neurol.* **71**, 505–508 (2014).
- Qiang, W., Yau, W. M. & Schulte, J. Fibrillation of β amyloid peptides in the presence of phospholipid bilayers and the consequent membrane disruption. *Biochim. Biophys. Acta Biomembr.* **1848**, 266–276 (2015).
- Delgado, D. A. et al. Distinct membrane disruption pathways are induced by 40-residue β -Amyloid peptides. *J. Biol. Chem.* **291**, 12233–12244 (2016).
- Qiang, W., Doherty, K. E., Klees, L. M. & Tobin-Miyaji, Y. Time-dependent lipid dynamics, organization and peptide-lipid interaction in phospholipid bilayers with incorporated β -amyloid oligomers. *J. Phys. Chem. Lett.* **11**, 8329–8336 (2020).
- Vander Zanden, C. M. et al. Fibrillar and nonfibrillar amyloid beta structures drive two modes of membrane-mediated toxicity. *Langmuir* **35**, 16024–16036 (2019).
- Lee, C. T. & Terentjev, E. M. Mechanisms and rates of nucleation of amyloid fibrils. *J. Chem. Phys.* **147**, 105103 (2017).
- Meisl, G. et al. Differences in nucleation behavior underlie the contrasting aggregation kinetics of the A β 40 and A β 42 peptides. *Proc. Natl. Acad. Sci. USA* **111**, 9384–9389 (2014).
- Srivastava, A. K. et al. β -Amyloid aggregation and heterogeneous nucleation. *Protein Sci.* **28**, 1567–1581 (2019).
- Thacker, D., Barghouth, M., Bless, M., Zhang, E. & Linse, S. Direct observation of secondary nucleation along the fibril surface of the amyloid. *Proc. Natl. Acad. Sci. USA* **120**, e2220664120 (2023).
- Press-Sandler, O. & Miller, Y. Molecular insights into the primary nucleation of polymorphic amyloid β dimers in DOPC lipid bilayer membrane. *Protein Sci.* **31**, e4283 (2022).
- Tycko, R. Symmetry-based constant-time homonuclear dipolar recoupling in solid state NMR. *J. Chem. Phys.* **126**, 64506–64506 (2007).
- Kenyaga, J. M., Cheng, Q. & Qiang, W. Early stage β -amyloid-membrane interactions modulate lipid dynamics and influence structural interfaces and fibrillation. *J. Biol. Chem.* **298**, 102491 (2022).
- Deo, T., Cheng, Q., Paul, S., Qiang, W. & Potapov, A. Application of DNP-enhanced solid-state NMR to studies of amyloid- β peptide interaction with lipid membranes. *Chem. Phys. Lipids* **236**, 105071 (2021).
- Qiang, W. et al. Heterotypic interactions between the 40- and 42-residue isoforms of β -amyloid peptides on lipid bilayer surfaces. *ACS Chem. Neurosci.* **14**, 4153–4162 (2023).
- Bak, M., Rasmussen, J. T. & Nielsen, N. C. SIMPSON: a general simulation program for solid-state NMR spectroscopy. 2000. *J. Magn. Reson.* **213**, 366–400 (2011).
- Orlikowska-Rzeznik, H., Krok, E., Chattopadhyay, M., Lester, A. & Piatkowski, L. Laurdan discerns lipid membrane hydration and cholesterol content. *J. Phys. Chem. B* **127**, 3382–3391 (2023).
- Yang, Y., Yao, H. & Hong, M. Distinguishing bicontinuous lipid cubic phases from isotropic membrane morphologies using $(31)\text{P}$ solid-state NMR spectroscopy. *J. Phys. Chem. B* **119**, 4993–5001 (2015).
- Otieno, S. A. & Qiang, W. Roles of key residues and lipid dynamics reveal pHLIP-membrane interactions at intermediate pH. *Biophys. J.* **120**, 4649–4662 (2021).
- Lau, T. L. et al. Amyloid-beta peptide disruption of lipid membranes and the effect of metal ions. *J. Mol. Biol.* **356**, 759–770 (2006).
- Schaefer, J. "Development of REDOR rotational-echo double-resonance NMR" by Terry Gullion and Jacob Schaefer. *J. Magn. Reson.* **213**, 421–422 (2011).
- Qiang, W., Yau, W.-M., Luo, Y., Mattson, M. P. & Tycko, R. Antiparallel beta-sheet architecture in lowa-mutant beta-amyloid fibrils. *Proc. Natl. Acad. Sci. USA* **109**, 4443–4448 (2012).
- Liu, C. et al. Out-of-register β -sheets suggest a pathway to toxic amyloid aggregates. *Proc. Natl. Acad. Sci. USA* **109**, 20913–20918 (2012).
- Gao, Y. et al. Out-of-register parallel β -sheets and antiparallel β -sheets coexist in 150-kDa oligomers formed by amyloid- $\beta(1-42)$. *J. Mol. Biol.* **432**, 4388–4407 (2020).
- Fatafta, H., Khaled, M., Owen, M. C., Sayyed-Ahmad, A. & Strodel, B. Amyloid- β peptide dimers undergo a random coil to β -sheet transition in the aqueous phase but not at the neuronal membrane. *Proc. Natl. Acad. Sci. USA* **118**, e2106210118 (2021).
- Potapov, A., Yau, W.-M., Ghirlando, R., Thurber, K. R. & Tycko, R. Successive stages of amyloid- β self-assembly characterized by solid-state nuclear magnetic resonance with dynamic nuclear polarization. *J. Am. Chem. Soc.* **137**, 8294–8307 (2015).
- Jeon, J., Yau, W. M. & Tycko, R. Early events in amyloid- β self-assembly probed by time-resolved solid state NMR and light scattering. *Nat. Commun.* **14**, 2964 (2023).
- Bahri, S. et al. H detection and dynamic nuclear polarization-enhanced NMR of A β . *Proc. Natl. Acad. Sci. USA* **119**, 2114413119 (2022).

36. Mentink-Vigier, F. et al. Computationally assisted design of polarizing agents for dynamic nuclear polarization enhanced NMR: the AsymPol family. *J. Am. Chem. Soc.* **140**, 11013–11019 (2018).
37. Harrabi, R. et al. Highly efficient polarizing agents for MAS-DNP of proton-dense molecular solids. *Angew. Chem. Int. Ed.* **61**, e202114103 (2022).
38. Wälti, M. A. et al. Atomic-resolution structure of a disease-relevant A β (1–42) amyloid fibril. *Proc. Natl. Acad. Sci. USA* **113**, E4976–E4984 (2016).
39. Yang, Y. et al. Cryo-EM structures of amyloid- β 42 filaments from human brains. *Science* **375**, 167–172 (2022).
40. Lee, M., Yau, W. M., Louis, J. M. & Tycko, R. Structures of brain-derived 42-residue amyloid- β fibril polymorphs with unusual molecular conformations and intermolecular interactions. *Proc. Natl. Acad. Sci. USA* **120**, e2218831120 (2023).
41. Lührs, T. et al. 3D structure of Alzheimer's amyloid-beta(1–42) fibrils. *Proc. Natl. Acad. Sci. USA* **102**, 17342–17347 (2005).
42. Xiao, Y. et al. A β (1–42) fibril structure illuminates self-recognition and replication of amyloid in Alzheimer's disease. *Nat. Struct. Mol. Biol.* **22**, 499–505 (2015).
43. Gremer, L. et al. Fibril structure of amyloid- β (1–42) by cryo-electron microscopy. *Science* **358**, 116–119 (2017).
44. Colvin, M. T. et al. High resolution structural characterization of A β 42 amyloid fibrils by magic angle spinning NMR. *J. Am. Chem. Soc.* **137**, 7509–7518 (2015).
45. Yang, J. et al. Differentiating A β 40 and A β 42 in amyloid plaques with a small molecule fluorescence probe. *Chem. Sci.* **11**, 5238–5245 (2020).
46. Kwak, S. S. et al. Amyloid- β 42/40 ratio drives tau pathology in 3D human neural cell culture models of Alzheimer's disease. *Nat. Commun.* **11**, 1377 (2020).
47. Cukalevski, R. et al. The A β 40 and A β 42 peptides self-assemble into separate homomolecular fibrils in binary mixtures but cross-react during primary nucleation. *Chem. Sci.* **6**, 4215–4233 (2015).
48. Tian, Y., Liang, R., Kumar, A., Szwedziak, P. & Viles, J. H. 3D-visualization of amyloid- β oligomer interactions with lipid membranes by cryo-electron tomography. *Chem. Sci.* **12**, 6896–6907 (2021).
49. Dey, A., Patil, A., Arumugam, S. & Maiti, S. Single-molecule maps of membrane insertion by amyloid- β oligomers predict their toxicity. *J. Phys. Chem. Lett.* **15**, 6292–6298 (2024).
50. Bitan, G. et al. Amyloid beta-protein (A β) assembly: A β 40 and A β 42 oligomerize through distinct pathways. *Proc. Natl. Acad. Sci. USA* **100**, 330–335 (2003).
51. Chang, H. W. et al. Site specific NMR characterization of A β 40 oligomers cross seeded by A β 42 oligomers. *Chem. Sci.* **13**, 8526–8535 (2022).
52. Dovidchenko, N. V. et al. One of the possible mechanisms of amyloid fibrils formation based on the sizes of primary and secondary folding nuclei of A β 40 and A β 42. *J. Struct. Biol.* **194**, 404–414 (2016).
53. Cheng, Q., Hu, Z. W., Doherty, K. E., Tobin-Miyaji, Y. J. & Qiang, W. The on-fibrillation-pathway membrane content leakage and off-fibrillation-pathway lipid mixing induced by 40-residue β -amyloid peptides in biologically relevant model liposomes. *Biochim. Biophys. Acta Biomembr.* **1860**, 1670–1680 (2018).
54. Cheng, Q. et al. Fibrillization of 40-residue β -amyloid peptides in membrane-like environments leads to different fibril structures and reduced molecular polymorphisms. *Biomolecules* **10**, 881 (2020).
55. Liao, S. Y., Lee, M., Wang, T., Sergeev, I. V. & Hong, M. Efficient DNP NMR of membrane proteins: sample preparation protocols, sensitivity, and radical location. *J. Biomol. NMR* **64**, 223–237 (2016).
56. Petkova, A. T. & Tycko, R. Sensitivity enhancement in structural measurements by solid state NMR through pulsed spin locking. *J. Magn. Reson.* **155**, 293–299 (2002).
57. Dubroca, T. et al. A quasi-optical and corrugated waveguide microwave transmission system for simultaneous dynamic nuclear polarization NMR on two separate 14.1T spectrometers. *J. Magn. Reson.* **289**, 35–44 (2018).

Acknowledgements

This work is supported by the National Institutes of Health (R01GM125853 to W.Q.) and the National Science Foundation (NSF-0922815) to the NMR facility at Binghamton University. A portion of this work was performed at the National High Magnetic Field Laboratory, which is supported by National Science Foundation Cooperative Agreement No. DMR-2128556 and the State of Florida. The MAS-DNP system at NHMFL is funded in part by NIH RM1-GM148766. F.J.S. acknowledges support from a postdoctoral scholar award from the Provost's Office at Florida State University.

Author contributions

W.Q., F.M.V. and T.W. designed research; M.K.K., J.M.K., P.X., X.W.H., J.W., B.L., Y.S., F.M.V., S.S.G., F.J.S. and W.Q. performed research; M.K.K., J.M.K. and W.Q. analyzed data; and M.K.K., F.W.V., T.W. and W.Q., wrote the paper.

Competing interests

The authors declare no competing interests.

Additional information

Supplementary information The online version contains supplementary material available at <https://doi.org/10.1038/s42004-025-01537-8>.

Correspondence and requests for materials should be addressed to Wei Qiang.

Peer review information *Communications Chemistry* thanks the anonymous reviewers for their contribution to the peer review of this work.

Reprints and permissions information is available at <http://www.nature.com/reprints>

Publisher's note Springer Nature remains neutral with regard to jurisdictional claims in published maps and institutional affiliations.

Open Access This article is licensed under a Creative Commons Attribution-NonCommercial-NoDerivatives 4.0 International License, which permits any non-commercial use, sharing, distribution and reproduction in any medium or format, as long as you give appropriate credit to the original author(s) and the source, provide a link to the Creative Commons licence, and indicate if you modified the licensed material. You do not have permission under this licence to share adapted material derived from this article or parts of it. The images or other third party material in this article are included in the article's Creative Commons licence, unless indicated otherwise in a credit line to the material. If material is not included in the article's Creative Commons licence and your intended use is not permitted by statutory regulation or exceeds the permitted use, you will need to obtain permission directly from the copyright holder. To view a copy of this licence, visit <http://creativecommons.org/licenses/by-nc-nd/4.0/>.

© The Author(s) 2025